Heliyon 9 (2023) e20911

Contents lists available at ScienceDirect

Heliyon

journal homepage: www.cell.com/heliyon

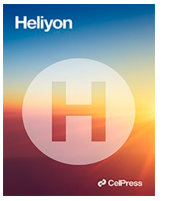

Intelligent computing for MHD radiative Von Kármán Casson nanofluid along Darcy-Fochheimer medium with activation energy

Muhammad Asif Zahoor Raja [a], Kottakkaran Sooppy Nisar [b,c,*], Muhammad Shoaib [d], Marwan Abukhaled [e], Aqsa Riaz [f]

[a] *Future Technology Research Center, National Yunlin University of Science and Technology, 123 University Road, Section .3, Douliou, Yunlin, 64002, Taiwan, ROC*
[b] *Department of Mathematics, College of Science and Humanities in Alkharj, Prince Sattam bin Abdulaziz University, 11942, Saudi Arabia*
[c] *School of Technology, Woxsen University, Hyderabad, 502345, Telangana State, India*
[d] *Yuan Ze University, AI Center, Taoyuan, 320, Taiwan, ROC*
[e] *Department of Mathematics and Statistics, American University of Sharjah, Sharjah, United Arab Emirates*
[f] *Department of Mathematics, University of Wah, Pakistan*

ARTICLE INFO

Keywords:
Von Karman's assertion
Bayesian Regularization technique
Radially extended rotating disc
Activation energy
MHD convective Casson nanofluid

ABSTRACT

The impact of activation energy in chemical processes, heat radiations, and temperature gradients on non-Darcian steady MHD convective Casson nanofluid flows (NMHD-CCNF) over a radial elongated circular cylinder is investigated in this study. The network of partial differential equations (PDEs) for NMHD-CCNF is developed using the modified Buongiorno framework, and the network of controlling PDEs is then transformed into ordinary differential equations (ODEs) utilizing the Von Karman method. Finally, the resulting non-linear ODEs are computed using the ND-solve approach to produce sets of data to assess the proposed model's skills, which can then be handled using the Bayesian Regularization technique of artificial neural networks (BRT-ANN). A novel stochastic computing-based application is being developed to evaluate the importance of NMHD-CCNF across a spinning disc that is radially stretched. The novelty and significance of results for better understanding, clarity, and highlighting the innovative contributions and significance of the proposed scheme. Further, to check the validity of the defined results for NMHD-CCNF, error charts, validation, and mean squared error suggestions are employed. The impact of multiple physical parameters on concentration, radial and tangential velocities, and temperature profiles is shown via tables and figures. Additionally, the results demonstrate that as the Forchheimer number, Casson nanofluid parameter, magnetic parameter, and porosity parameter are strengthened, the radial and rotational nanofluid mobility drops dramatically. The stretching parameter, on the other hand, has a parallel developmental trend. The heat generation parameter, the thermophoresis process, the thermal radiation parameter, and the Brownian motion of nanoparticles can all be increased to give thermal enhancement. On the other side, with larger estimates in thermophoresis parameters and the activation energy, there is a noticeable increase in the concentration profile.

* Corresponding author. Department of Mathematics, College of Science and Humanities in Alkharj, Prince Sattam bin Abdulaziz University, 11942, Saudi Arabia.

E-mail addresses: rajamaz@yuntech.edu.tw (M.A.Z. Raja), n.sooppy@psau.edu.sa (K.S. Nisar), dr.shoaib@saturn.yzu.edu.tw (M. Shoaib), mabukhaled@aus.edu (M. Abukhaled), aqsar9703@gmail.com (A. Riaz).

https://doi.org/10.1016/j.heliyon.2023.e20911
Received 3 October 2022; Received in revised form 8 October 2023; Accepted 11 October 2023
Available online 13 October 2023

Nomenclature

u, v, w	Velocity components $(m.s^{-1})$
υ	kinematic viscosity $(m^2.s^{-1})$
p	Pressure $(Pa.s)$
M	Magnetic parameter
Sc	Schmidt number
Rd	Thermal radiation parameter
F_r	Forchheimer number
Nt	Thermophoresis parameter
Λ	chemical reaction parameter
$L(\eta), F(\eta), G(\eta)$	Dimensionless velocity components
$r(m), \varphi(rad), z(m)$	Cylindrical coordinates
Pr	Prandtl number
Sh	Sherwood number
Nu	Nusselt number
Γ	Temperature difference parameter
K_c	Chemical reaction rate constant (s^{-1})
k_B	Boltzmann constant $(J.K^{-1})$
n	Fitted rate constant
p_y	Casson yield stress (Pa)
a	Stretching parameter
β	Casson parameter
P	Porosity parameter
Q_T	Heat generation parameter
Nb	Brownian motion parameter
$\theta(\eta)$	Dimensionless temperature
$\varphi(\eta)$	Dimensionless concentration
Re_r	Local Reynolds number
E	Activation energy parameter $(J.K^{-1})$
q_m	Mass flux $(kg.m^{-2}.s^{-1})$
K	Permeability (m^2)
BRT-ANN	Bayesian Regularization Technique of Artificial Neural Networks
NMHD-CCNF	Non-Darcian steady magnetohydrodynamic Convective Casson Nanofluid Flows

1. Introduction

Swedish scientist 'Svante Arrhenius' coined "activation energy," meaning "the minimum amount of energy required to initiate a chemical process," in 1889. Oil container design, food manufacturing, synthetical processing, oil coating, and other operations all involve mass transfer with activation energy. There are active systems that use chemical substances to activate reactions and create a large amount of production. Arrhenius [1] monitors the reaction rate using activation energy as a chemical indicator. Most reactants need a lot of energy to overcome a reaction shield. As a result, numerous chemical changes can't go forward effectively until the reactants reach a certain energy level. In these cases, the Arrhenius activation energy is associated with energy variation between the regions and reactants. Bestman et al. [2] evaluated the influence of Arrhenius activation energy in the passage of a flammable gas through a vertical cylinder in 1991. Mullin et al. [3] investigated basic ideas about Arrhenius rates using analytical and empirical data. Shoaib et al. analyze the ferrofluid flow model's magnetic field and heat source impacts [4]. The flowing and activation energy distribution among a set of turning circular surfaces filled with Carreau fluid is considered by Arain [5]. Shoaib [6] explored the Ohmic heating effects and energy formation in a Ree-Eyring fluid nanofluidic setup. Jensen et al. [7] demonstrated the levels of energy of breakdown and thermodynamic estimates of the temperature and heat of explosion for seventy strong compounds utilizing Density Functional Theory. Waqas et al. [8] explored the influence of thermal emission and energy of activation on the mixed convection flowing of a third grade nanofluid including swimming organisms across a stretched sheet in the presence of a heat source-sink. Zhang et al. [9] looked at the dynamics of nanofluids on a nonlinear permeable extended sheet with Lorentz forces and Arrhenius rates. Abdul Maleque [10–12] examined the impact of chemical processes with Arrhenius activation energy on dynamic convection heat and mass transfer boundary layer fluid flow, among other discoveries. Olanrewaju [13] studies the thermodynamic second law of an Arrhenius kinetic species with a coupled Maxwell magneto-nanofluid in porous material. Bhatti et al. found that magnetic field effect decreases entropy in a porous mobile sheet of Powell-Eyring nanofluid flow [14]. It was discovered that heat generation is an increasing function for all physical quantities studied.

Centrifugal compressors, air purification devices, food manufacturing, storage systems, thermal power generation systems, and a variety of other moving mechanical devices all experience flow patterns powered by a circular cylinder. Von Karman [15] was a founder who used the elegant similarity transformation to minimize the leading equations into a set of ordinary differential equations to analyze the flow model over a revolving disc, it was eventually dubbed the Von Karman circling disc movement in principle because of the pioneering efforts. Anderson et al. [16] explored the Von Kármán spinning movement of a non-Newtonian power-law fluid across a circling disc with the new precise power-law indices range of 1.5–2.0 and found comparable answers. The heat flow of Cattaneo-Christov, the Von Kármán circling flow issue, is expanded for Navier's slip circumstance on the stretched spinning disc media [17].

A few researchers were reporting issues with the Casson fluid framework owing to suitable estimations for a variety of biological and specific real solutions, like melting chocolate, orange juice, and sauces prepared with tomatoes. The Casson fluid displays yield stress, and once the applied shear stress is larger than the yield stress, the fluid acts as a Newtonian fluid. The fluid acts like an elastic solid when the yield stress is larger than the shear stress [18]. Using Navier's slip condition, they investigated the concentration, velocity, and temperature field of a Casson fluid flow across a spiraling disc. Permeable medium, which has various applications in the food industry, construction, and industrial operations [19], seems to be an additional medium that regulates the passage of heat and fluid velocity. Although Darcy's law has historically illustrated the flow features of this medium, the expanded Darcy-Forchheimer framework is commonly used for flow with greater speed.

The modified permeable law can be referred to as Darcy-porous Forchheimer's model or non-porous Darcy's model, depending on the history of the porosity framework since the eighteenth century. Furthermore, the structure of pore spaces in a medium has promising applications in a variety of fields (for example, textiles, environmental safety, chemical filtration, electrical and chemical batteries, fuel cells, geotechnical engineering, biophysics, ecotoxicity analyses, and petroleum engineering). In addition to the occurrence of ohmic dispersion and a non-uniform source or sink of heat, other noteworthy nanofluid flow findings were clarified in Refs. [20–29] for diverse geometrical configurations and physical restrictions.

Numerous mathematical and computational methods were implemented in recent years for the computational analysis of complex problems under variable circumstances, such as regular perturbation [30], differential evolution algorithm [31], HAM [32], and ADM [33], but artificial neural networking is the most productive mathematical approach because it provides a higher convergence rate and lower mean square errors. In a variety of domains, probabilistic mathematical computing-based algorithms employing neural network models are used to resolve linear as well as nonlinear differential equations. Artificial neural networks (ANN) can manage large data samples, implicitly identify complicated dynamic associations between dependent and independent variables, recognize all regression model connections, etc. In conclusion, ANNs are highly adaptive and effective. They can simulate any complex task since they are universal function models. Ongoing studies on intelligent computing structure emphasize stochastic strategies in ferrofluid flow through exponentially stretched sheets with thermal energy [34], entropy optimization [35], plasma models [36], fluid dynamic models [37–39] and reactive transport model [40].

The above citations indicate the presence of numerous studies on the 2D or 3D convective flow pattern of Newtonian or non-Newtonian nanofluids passing nearby geometrical designs on a plane, whose calculated explanation has been constructed using a Cartesian frame linked to the observed data. The study of mass and heat transport phenomena associated with magnetohydrodynamic responsive Von Kármán streams of Casson nanofluids across an isothermal elongated rotating cylinder is quite lacking in nanofluids research, and it has however to be addressed thoroughly in the context of Buongiorno's two-phase methodology [41] and the energetic controller scheme. Interested readers can refer to the following papers on fluid flow and heat transfer related studies [55–58].

The existence of non-linear thermal flows and the participation of a temperature-dependent source of heat, as well as the resistant influence of Darcy-Forchheimer and Lorentz drag forces, add to the originality of the current numerical analysis. The leading borderline layer comparisons are generated depending on acceptable, precise conversions and reasonable somatic considerations by adding the activation energy impact. After that, the nonlinear differential equations are simply calculated using the ND-solve approach to provide sets of data for BRT-ANN. In addition, the collected ND-solve datasets are tabulated and visually shown to give a deeper practical understanding of the flow pattern and the consequent transport processes using the current radiative-reactive nanofluids system. In this study, we observe that both tangential and radial velocity profiles decrease with the increase in values of the Forchheimer number, magnetic parameter, and porosity parameter, and both tangential and radial velocity patterns decrease with the rise in values of the Casson parameter. With rising values of the stretching parameter, radial velocity increases, whereas tangential velocity decreases. The temperature profile is improved by the thermal radiation and heat generation parameters. In temperature and concentration profiles, has the opposite impact. As the value rises, so do the temperature and concentration profiles. The concentration profile decreases as it increases, although the Arrhenius activation energy parameter increases significantly. The local skin friction coefficient is dominated by non-Darcian phenomena, which include parameters like P and F_r. The greater the value of Rd, the better the rate of heat transmission through the wall. As the value of parameter E increases, the rate of wall mass transfer decreases.

Mathematica (version 12) and MATLAB (version R2019b) are used in this work for the numerical method. The following are the key objectives of the ongoing investigation:

- A novel stochastic computing-based procedure is being developed to evaluate the importance of NMHD-CCNF across a spinning disc that is radially stretched.
- The training, testing, and validation procedures are used to assess the anticipated solutions for NMHD-CCNF.
- Investigate and compare the estimated results of generated BRT-ANNs to prescribed data solutions utilizing training/validation datasets/testing.
- To describe how analyses of regression indices, histogram of errors, and MSE graphs were used to quantify increased performance.

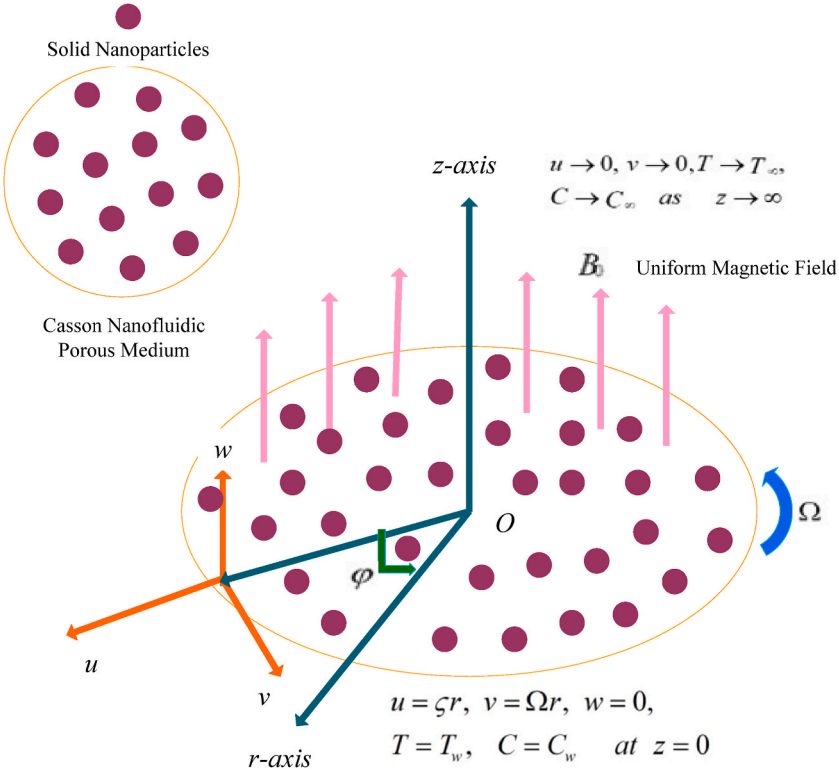

Fig. 1. Flow diagram.

- Modifying important elements to investigate distinct NMHD-CCNF conditions.
- Supervised ANN technique was used in this experiment.

This paper will be organized as follows: Section 2 shows how to formulate the issue using governing differential equations. Section 3 presents the Artificial Neural Network modelling effort, as well as the graphs and tables examining the proposed model. The current findings are described in Section 4. We further compare the acquired results to recently published papers in Section 4. Lastly, in Section 5, deductions have been derived.

2. Problem formulation

We take into account a Casson nanofluid in a three-dimensional magnetohydrodynamic convective non-Newtonian flow over a stretchy revolving plate that is heated isothermally, and turn the disc proportionally with angular velocity Ω along z-axis, axially at a consistent rate ς, and horizontally in a Darcy-Forchheimer permeable system as shown graphically in Fig. 1. The factors of (u,v,w) also describe the velocity of the Casson nanofluid, that displays the motion, in cylindrical coordinates (r,φ,z). The flow of this Casson nano - fluid is accelerated at the magnetic flux to achieve a constant transverse magnetic field B_o, the thermal flow is enlarged in the presence of nonlinear radiant flow with an internally thermal cause of heat, and the chemical flow is increased by Arrhenius kinetics. The temperatures of the barrier wall and flowing stream are given by T_w and T_∞ respectively, and its concentrations were symbolically expressed by C_w and C_∞.

The PDE that depicts the flow structure for a proposed system in the exclusion of magnetic phenomena are shown as follows [20,44,45] using the concept of boundary layer theory [42] and Buongiorno's model [43].

$$\frac{\partial u}{\partial r}+\frac{u}{r}+\frac{\partial w}{\partial z}=0, \tag{1}$$

$$\frac{\partial u}{\partial r}u-\frac{v^2}{r}+\frac{\partial u}{\partial z}w=-\frac{\partial p}{\partial r}\frac{1}{\rho}+\frac{\upsilon(\beta+1)}{\beta}\left(\frac{\partial^2 u}{\partial r^2}+\frac{1}{r}\frac{\partial u}{\partial r}-\frac{u}{r^2}+\frac{\partial^2 u}{\partial z^2}\right)-\frac{\sigma B_0^2}{\rho}u-\frac{\upsilon}{K}u-\frac{C_b}{r\sqrt{K}}u^2, \tag{2}$$

$$u\frac{\partial v}{\partial r}+\frac{uv}{r}+w\frac{\partial v}{\partial z}=\frac{\upsilon(\beta+1)}{\beta}\left(\frac{\partial^2 v}{\partial r^2}+\frac{1}{r}\frac{\partial v}{\partial r}-\frac{v}{r^2}+\frac{\partial^2 v}{\partial z^2}\right)-\frac{\sigma B_0^2}{\rho}v-\frac{\upsilon}{K}v-\frac{C_b}{r\sqrt{K}}v^2, \tag{3}$$

$$\frac{\partial w}{\partial r}u+\frac{\partial w}{\partial z}w=-\frac{\partial p}{\partial z}\frac{1}{\rho}+\frac{\upsilon(\beta+1)}{\beta}\left(\frac{\partial^2 w}{\partial r^2}+\frac{\partial w}{\partial r}\frac{1}{r}+\frac{\partial^2 w}{\partial z^2}\right), \tag{4}$$

$$\begin{aligned}\frac{\partial T}{\partial r}u+\frac{\partial T}{\partial z}w=&\frac{k}{\rho C_p}\left(\frac{\partial^2 T}{\partial r^2}+\frac{\partial^2 T}{\partial z^2}+\frac{1}{r}\frac{\partial T}{\partial r}\right)+\frac{D_B\left(\rho C_p\right)_s}{\delta_c\left(\rho C_p\right)}\left(\frac{\partial C}{\partial r}\frac{\partial T}{\partial r}+\frac{\partial C}{\partial z}\frac{\partial T}{\partial z}\right)+\frac{D_T\left(\rho C_p\right)_s}{T_\infty\left(\rho C_p\right)}\\&\left\{\left(\frac{\partial T}{\partial r}\right)^2+\left(\frac{\partial T}{\partial z}\right)^2\right\}+\frac{Q}{\rho C_p}(T-T_\infty)-\frac{1}{\rho C_p}\frac{\partial q_r}{\partial z},\end{aligned} \tag{5}$$

$$\begin{aligned}u\frac{\partial C}{\partial r}+w\frac{\partial C}{\partial z}=&D_B\left(\frac{\partial^2 C}{\partial r^2}+\frac{\partial^2 C}{\partial z^2}+\frac{1}{r}\frac{\partial C}{\partial r}\right)+\frac{D_T\delta_c}{T_\infty}\left(\frac{\partial^2 T}{\partial r^2}+\frac{\partial^2 T}{\partial z^2}+\frac{1}{r}\frac{\partial T}{\partial r}\right)\\&-K_c\left(\frac{T}{T_\infty}\right)^n\exp\left(\frac{-E_\alpha}{k_B T}\right)(C-C_\infty),\end{aligned} \tag{6}$$

The following are the relevant boundary conditions for the system of PDEs along the surface of the plate and away from the surface:

$$u=\varsigma r, w=0, v=\Omega r, C=C_w, T=T_W \quad at \quad z=0, \tag{7}$$

$$u\to 0, T\to T_\infty, v\to 0, C\to C_\infty \quad as \quad z\to\infty.$$

The Rosseland technique [46] is used to compute the heat flow in the z-direction.

$$q_r=-\frac{4\sigma^*}{3k^*}\left(\frac{\partial T^4}{\partial z}\right)=-\frac{16\sigma^*}{3k^*}\left(T^3\frac{\partial T}{\partial z}\right). \tag{8}$$

The PDEs (1–6) and their accompanying boundary conditions (7–8) are reformed into ODEs using the Von Karman similarity transformation given in (9), (Also, see Refs. [47,48]).

$$\left.\begin{aligned}&u=\Omega rL(\eta), v=\Omega rF(\eta), w=(\Omega\upsilon)^{\frac{1}{2}}G(\eta), \eta=\left(\frac{\Omega}{\upsilon}\right)^{\frac{1}{2}}z,\\&p-p_\infty=2\mu\Omega H(\eta), \varphi(\eta)=\frac{C-C_\infty}{C_w-C_\infty}, \theta(\eta)=\frac{T-T_\infty}{T_w-T_\infty}.\end{aligned}\right\} \tag{9}$$

For the suggested NMHD-CCNF, ODEs with boundary conditions are mentioned below.

$$2L+G'=0, \tag{10}$$

$$\left(\frac{\beta+1}{\beta}\right)L''-(M+P)L-GL'-(1+Fr)L^2+F^2=0, \tag{11}$$

$$\left(\frac{\beta+1}{\beta}\right)F''-(M+P)F-GF'-2LF-FrF^2=0, \tag{12}$$

$$\begin{aligned}\theta''+\Pr Q_T\theta+Rd(1+\Gamma\theta)^3\theta''+3Rd\Gamma(1+\Gamma\theta)^2\theta'^2+N_t\theta'^2+N_b\theta'\varphi'\\-\Pr G\theta'+\Pr N_b\theta'\varphi'+\Pr N_t=0,\end{aligned} \tag{13}$$

$$\varphi''-ScG\varphi'+\frac{N_t}{N_b}\theta''-Sc\Lambda(1+\Gamma\theta)^n\exp\left(\frac{-E}{1+\Gamma\theta}\right)\varphi=0, \tag{14}$$

subjected boundary conditions are,

$$\left.\begin{aligned}&L(\eta)=a, F(\eta)=1, G(\eta)=0, \theta(\eta)=1, \varphi(\eta)=1 \quad as \quad \eta\to 0,\\&L(\eta)=0, F(\eta)=0, \theta(\eta), \varphi(\eta)\to 0 \quad as \quad \eta\to\infty.\end{aligned}\right\} \tag{15}$$

Here n is the fitted rate constant, β shows the Casson parameter, P is porosity parameter, F_r represents the Forchheimer number, M is the magnetic parameter, Pr denotes the Prandtl number, N_t denotes the thermophoresis parameter, N_b is Brownian parameter, Q_T indicates heat generation parameter, Γ is temperature differences parameter, Rd is thermal radiation parameter, Sc denotes the Schmidt number, Λ denotes the chemical reactive factor, E is active energy parameter and a represents stretching parameter. These parameters are characterized by:

$$\beta=\frac{\mu\sqrt{2\pi_c}}{p_y}, P=\frac{\upsilon}{K\Omega}, F_r=\frac{C_b}{(K)^{1/2}}, M=\frac{\sigma{\beta_0}^2}{\rho\,\Omega}, \mathrm{Pr}=\frac{\upsilon}{\alpha},$$

$$N_t=\frac{(\rho C_p)_s D_T(T_w-T_\infty)}{\upsilon(\rho C_p)T_\infty}, N_b=\frac{(\rho C_p)_s D_B(C_w-C_\infty)}{\upsilon(\rho C_p)\delta_C}, Q_T=\frac{Q}{\Omega(\rho C_p)},$$

$$\Gamma=\frac{(T_w-T_\infty)}{T_\infty}, Rd=\frac{16\sigma^* {T_\infty}^3}{3kk^*}, Sc=\frac{\upsilon}{D_B}, \Lambda=\frac{K_c}{\Omega}, E=\frac{E_a}{k_b T_\infty}, a=\frac{\varsigma}{\Omega}$$

$$u=\varsigma r, w=0, v=\Omega r, T=T_W, C=C_W \quad at \quad z=0,$$

The dimensionless formulations of the total viscous frictional factor C_{fr}, the wall thermal transfer rate Nu_r, and the wall mass transport rate Sh_r are specifically provided accurately by:

$$C_{fr}=\frac{\left(\tau_{w\varphi}^2+\tau_{wr}^2\right)^{1/2}}{(r\Omega)^2\rho}, \tag{16}$$

$$Nu_r=\frac{q_h r}{(T_w-T_\infty)k}, \tag{17}$$

$$Sh_r=\frac{\delta_C q_m r}{(C_w-C_\infty)D_B\rho_s}. \tag{18}$$

Furthermore, the following formulas apply to the related shear stress components $(\tau_{wr},\tau_{w\varphi})$, in addition to heat and mass fluxes (q_h,q_m):

$$\tau_{wr}=\mu\left(\frac{\partial w}{\partial r}+\frac{\partial u}{\partial z}\right)_{z=0},$$

$$\tau_{w\varphi}=\mu\left(\frac{1}{r}\frac{\partial w}{\partial \varphi}+\frac{\partial v}{\partial z}\right)_{z=0},$$

$$q_h=-\left(\frac{\partial T^4}{\partial z}\frac{4\sigma^*}{3k^*}+\frac{\partial T}{\partial z}k\right)_{z=0},$$

$$q_m=-\frac{D_B\rho_s}{\delta_C}\left(\frac{\partial C}{\partial z}\right)_{z=0}.$$

We get the following reduced versions by simplifying equations 16–18:

$$C_f=\left(\frac{\beta+1}{\beta}\right)\left(\sqrt{(L')^2+(F')^2}\right)_{\eta=0},$$

$$Nu=-\left(1+Rd[1+\Gamma\theta(0)]^3\right)(\theta')_{\eta=0},$$

$$Sh=-(\varphi')_{\eta=0},$$

where

$$C_f=\mathrm{Re}_r^{1/2}C_{fr}, Nu=\mathrm{Re}_r^{-1/2}Nu_r, Sh=\mathrm{Re}_r^{-1/2}Sh_r, \mathrm{Re}_r=\frac{\Omega r^2}{\upsilon}.$$

3. Solution methodology

This study uses BRT-ANN to examine how activation energy during chemical processes, thermal radiation, and temperature gradient affect NMHD-CCNF over a revolving axially elongated disc. PDEs are converted to ODEs using the required transformations. Adam numerical approach is implemented through 'ND Solve' function available in the Mathematica for answering the ordinary differential equations. The neural network is generated based on reference data taking the domain 0 and 4 for variants associated with the presented fluid flow system.

3.1. Adams numerical method

The following is an expression of Adams's numerical technique for a first-order system:

$$\frac{dy}{dx}=F(x,y),$$

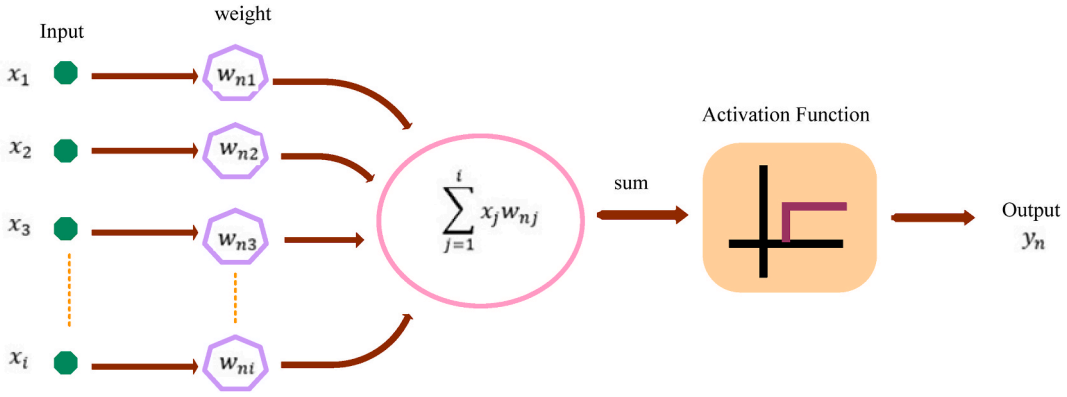

Fig. 2. A layout of singular neural networking of model.

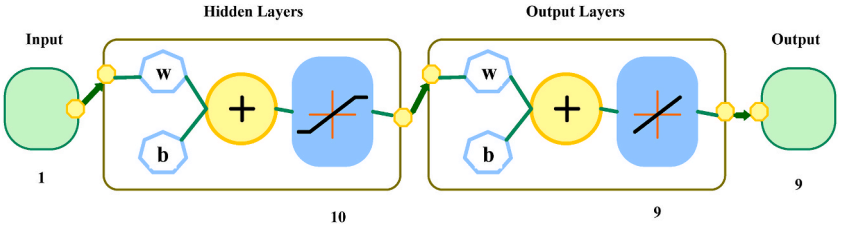

Fig. 3. A suggested neural network's design.

Table 1
Variation of parameters of (NMHD-CCNF).

Scenarios	Cases	Physical Quantities										
		a	P	M	β	F_r	Nt	Nb	Q_T	Λ	Rd	E
01	**1**	1.0	0.5	0.5	0.3	0.5	0.7	0.5	0.1	0.5	1.0	0.5
	2				0.5							
	3				0.7							
02	**1**					0.4						
	2					0.9						
	3					1.4						
03	**1**								0.1			
	2								0.4			
	3								0.7			
04	**1**									0.6		
	2									1.2		
	3									1.8		
05	**1**										0.6	
	2										1.2	
	3										1.8	
06	**1**											0.2
	2											0.6
	3											1.1

$$Y_{k+1} = y_k + \int_{t_k}^{t_{k+1}} \frac{dy}{dx}\, dt = y_k + \int_{t_k}^{t_{k+1}} F(y,t)\, dt,$$

where y characterizes the outcome of a linear first-order ODE, x is the data input, Y_{k+1} denotes the first-order interpolated iterative method and the time period represented by t.

Adams' methods are predicated on approximating the integral inside the interval (t_k, t_{k+1}) with a polynomial. Adams' methods come in two different types: explicit and implicit forms. The Adams-Bashforth (AB) approach is the explicit type, and the Adams-Moulton (AM) approach is the implicit type. The first-order AB and AM approaches are forward and backward Euler methods. The

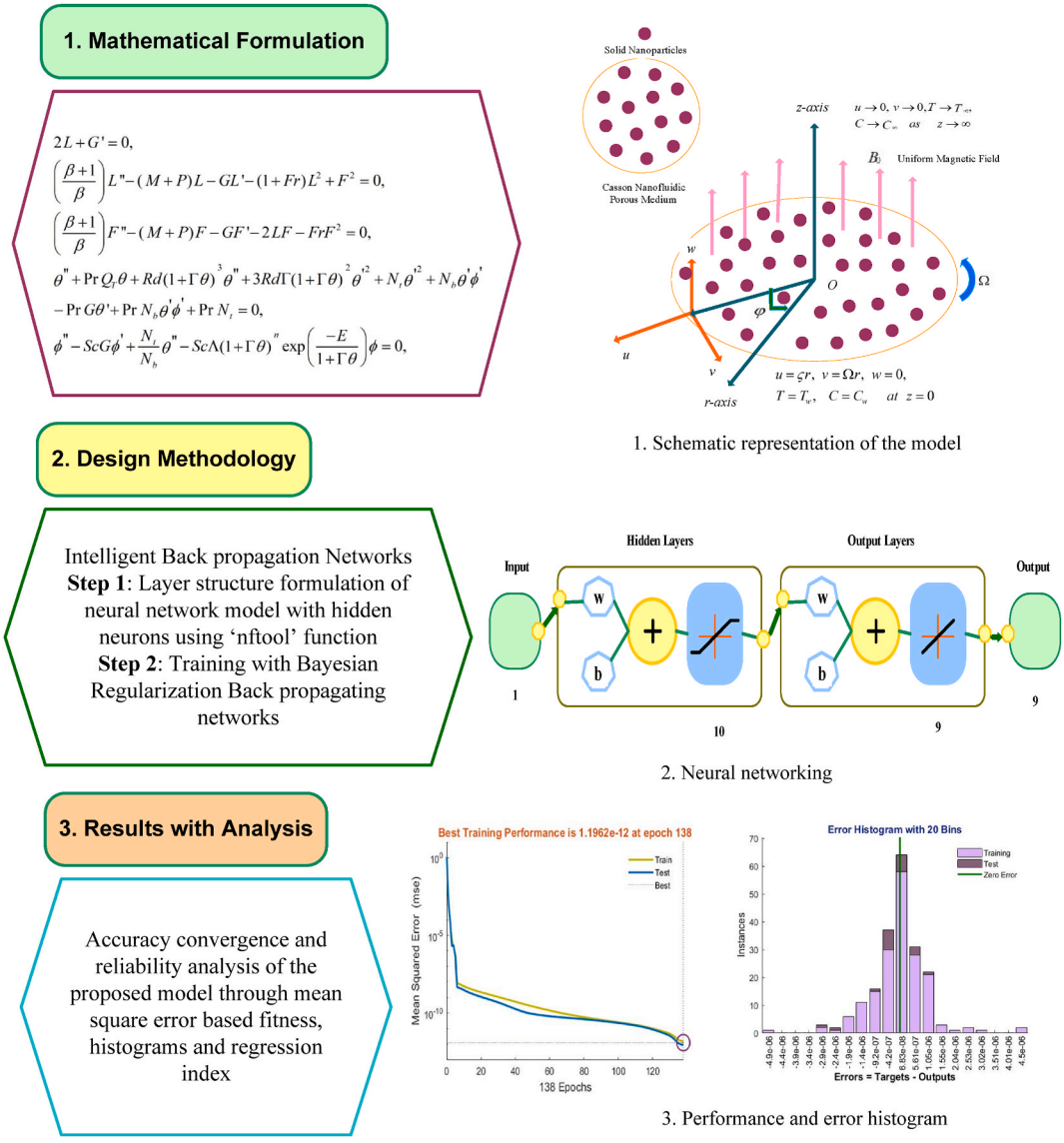

Fig. 4. Suggested BRT-ANN processing for NMHD-CCNF model.

linear interpolant-derived second-order iterations of these methods are widely used. The second-order Adams-Bashforth (AB2) method is explained in equation (19).

$$Y_{k+1}=y_k+\frac{q}{2}\left(3F(y_k,t_k-F(y_{k-1},t_{k-1})\right), \tag{19}$$

here q is the step spacing. Adams-Moulton's second order (AM2) is an implicit method also referred to as the trapezoidal notion is

$$Y_{k+1}=y_k+\frac{q}{2}\left(F(y_{k+1},t_{k+1}+F(y_k,t_k)\right).$$

Adam numerical approach is implemented through 'ND-Solve' function available in the Mathematica environment for the solution of ordinary differential equations. The neural network is generated on the basis of reference data taking the domain 0 and 4 for variants associated with the presented fluid flow system The Proposed Neural Network approach is implemented in MATLAB software by implementing the ND-solve technique using default settings for iterations, accuracy objective, and acceptance rate for answering ordinary mathematical equations, and then by using the NF-tool (neural network fitting tool) on a similar pattern as reported in Refs. [50–54].

Fig. 2 illustrates a single neural network model. Here, BRT-ANN is built using NF-tool in MATLAB with suitable parameters of unseen neurons, testing dataset, training dataset, and validation dataset, while the suggested network's topology is shown in Fig. 3.

Table 2
Outcomes of BRT-ANN of NMHD-CCNF.

Scenario	Case	MSE data		Performance	Gradient	Mu	Final Epoch	Time
		Training	Testing					
01	**1**	1.28367E-13	2.08283E-13	1.28E-13	2.49E-09	5000	219	<1s
	2	5.17130E-13	5.31211E-13	5.17E-13	9.38E-09	5000	100	2s
	3	9.94063E-12	2.18445E-11	9.94E-12	3.73E-08	5000	88	2s
02	**1**	3.16751E-12	3.89762E-12	3.17E-12	2.65E-08	5000	136	1s
	2	2.26968E-13	2.11283E-12	2.27E-13	3.63E-09	5000	410	1s
	3	1.32695E-12	1.40816E-12	1.33E-12	9.25E-09	5000	163	3s
03	**1**	2.25598E-12	3.09567E-12	2.26E-12	8.26E-08	5000	148	2s
	2	6.84999E-13	1.42956E-12	6.85E-13	2.74E-08	5000	67	1s
	3	4.17639E-13	4.28696E-13	4.18E-13	9.59E-08	5000	161	2s
04	**1**	4.15304E-12	8.51828E-12	4.15E-12	2.84E-08	500	141	1s
	2	2.23624E-12	4.88588E-12	2.24E-12	1.63E-08	500	151	<1s
	3	4.05286E-12	5.08361E-12	4.05E-12	2.21E-08	500	174	<1s
05	**1**	7.41853E-10	3.21520E-09	7.42E-10	4.29E-08	500	82	<1s
	2	4.73777E-12	6.76567E-12	4.74E-12	8.86E-08	500	102	<1s
	3	1.90470E-12	2.40125E-12	1.90E-12	9.80E-08	500	175	<1s
06	**1**	3.62361E-12	4.66304E-12	3.62E-12	2.36E-08	500	141	<1s
	2	3.91196E-12	3.59056E-12	3.91E-12	2.55E-08	500	159	<1s
	3	3.58251E-12	4.39716E-12	3.58E-12	2.09E-08	500	94	2s

Using Bayesian Regularization backpropagation, software is utilized to train the weight function of a neural network. The proposed BRT-ANN combines a multi-layer neural network structure with Bayesian Regularization backpropagation for optimization. For eleven scenarios, numerical solutions are gained by NF-tool for the model of MHD Casson nanofluidic expressed in equation 10–15 by varying, $\beta, F_r, Q_T, \Lambda, Rd, and\ E$, each with three cases with defaults values as,

$$\beta = 0.5, F_r = 0.5, Q_T = 0.1, \Lambda = 0.5, Rd = 1.0, and\ E = 0.5 \text{ while } a = 1, P = 0.5, M = 0.5, N_t = 0.7, N_b = 0.5, n = 0.5, \Gamma = 0.2, Sc = 0.5, \Pr = 7 \text{ are kept fixed.}$$

The place values for BRT-ANN are developed with a scaling factor of 0.04 with input ranging from 0 to 4 using Mathematica ND-solve approach. Table 1 lists the descriptions of every scenario of the MHD Casson nanofluidic flow model. By using NF-tool with 10 neurons in the hidden layer and datasets for learning, verification, and evaluation 80 %, 10 %, and 10 % respectively, the intended BRT-ANN procedure is imposed to find results of a steady 3-D MHD Casson nanofluidic flow system. Fig. 4 also shows the process map of the completed BRT-ANN.

The plots for $L(\eta), F(\eta)$, $\theta(\eta)$ and $\varphi(\eta)$ are depicted in the figures. Table 1 also includes physical quantity change scenarios and conditions which illustrate the NMHD-CCNF. Data sets are created for training, testing, and validation, and may be utilized to assess the model's expected outcomes. Table 2 displays the answers of the number of experiments depending on back-propagation networks, iterations, MSE, and time connection for all the NMHD-CCNF cases. MSE plots, regression, and histograms of error analysis all verify the fantastic work test results of NMHD-CCNF using BRT-ANN.

Fig. 5 displays the predicted the validity of convergence, trained data, and evaluated gains over epochs indexes for created BRT-ANN for confronting the scenarios of $\beta, F_r, Q_T, \Lambda, Rd, and\ E$ for $L(\eta), F(\eta), \theta(\eta)$ and $\varphi(\eta)$ of NMHD-CCNF. The required performance is achieved in 219, 100, 88, 136, 163, 148, 67, 161, 141, 151, 174, 102, 175, and 141 iterations in total time of <1s, 2s, 2s, 1s, 3s, 2s, 1s, 2s, 1s, <1s, <1s, <1s, <1s, and <1s. Fig. 5 shows the impact of error dynamics analysis on error histograms. For the cases of $\beta, F_r, Q_T, \Lambda, Rd, and\ E$ for $L(\eta), F(\eta), \theta(\eta)$ and $\varphi(\eta)$ of NMHD-CCNF, an inspection of the error histogram reveals a large number of error values lying over the zero axis, as well as an error box of reference. Fig. 6 illustrate the converging capacity and accuracy, as well as fitness curves, for the scenarios of $\beta, F_r, Q_T, \Lambda, Rd, and\ E$ for $L(\eta), F(\eta), \theta(\eta)$ and $\varphi(\eta)$ of NMHD-CCNF. 2.49E-09, 9.38E-09, 3.73E-08, 2.65E-08, 9.25E-09, 8.26E-08, 2.74E-08, 9.59E-08, 2.84E-08, 1.63E-08, 2.21E-08, 8.86E-08, 9.80E-08, and 2.36E-08 are the corresponding gradient values for best performance. Mu parameter 5000, 5000, 5000, 5000, 5000, 5000, 5000, 5000, 500, 500, 500, 500, 500, and 500 of BRT-ANN is as shown. Furthermore, the picture shows that an increase in iterations lowers both gradient and Mu. The higher the network's testing and training, the higher the convergence for minimal Mu and gradient. Fig. 7 depicts the regression for all data, together with training, testing, and validation. It was revealed throughout the analysis that the results and desired values have a regression value of R = 1.

4. Discussions

The MATLAB software is used to determine the consequences of different values of $\beta, F_r, Q_T, \Lambda, Rd, and\ E$ for $L(\eta), F(\eta), \theta(\eta)$ and $\varphi(\eta)$ of NMHD-CCNF. Figs. 8–11 shows the BRT-ANN results of the NMHD-CCNF model for velocities, temperature, and concentration profiles, as well as their AE analysis graphs. The exact error values for the relevant variants are 10^{-5} to 10^{-9}, 10^{-5} to 10^{-9}, 10^{-5} to 10^{-8}, 10^{-5} to 10^{-9}, 10^{-5} to 10^{-9}, 10^{-4} to 10^{-8}, 10^{-5} to 10^{-9}, 10^{-5} to 10^{-8}.

This axial portion focuses on the magnetohydrodynamic convection of Casson nanofluids pushed across an elongated rotating disc that is positioned horizontally within a Darcy-Forchheimer permeable channel, warmed at constant temperature, and managed

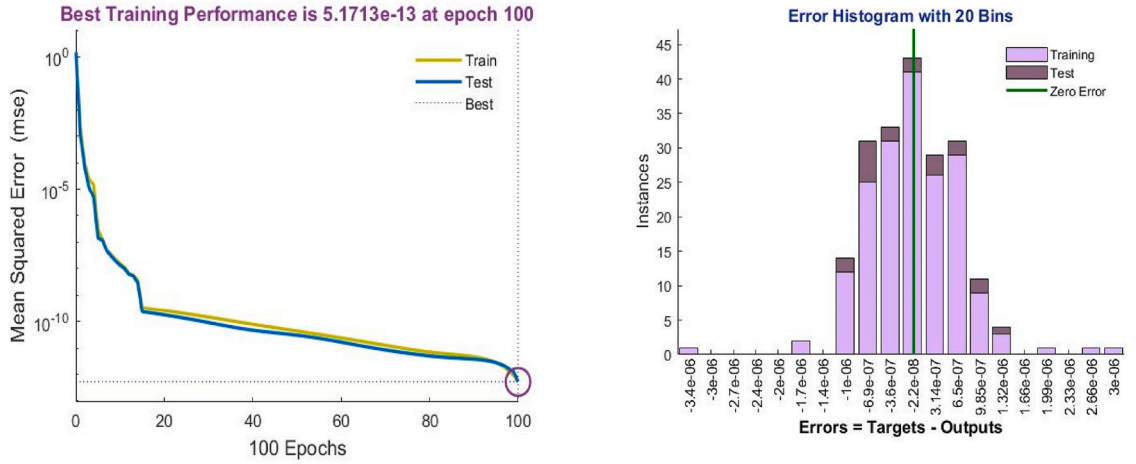

a. Scenario 1 Case 2

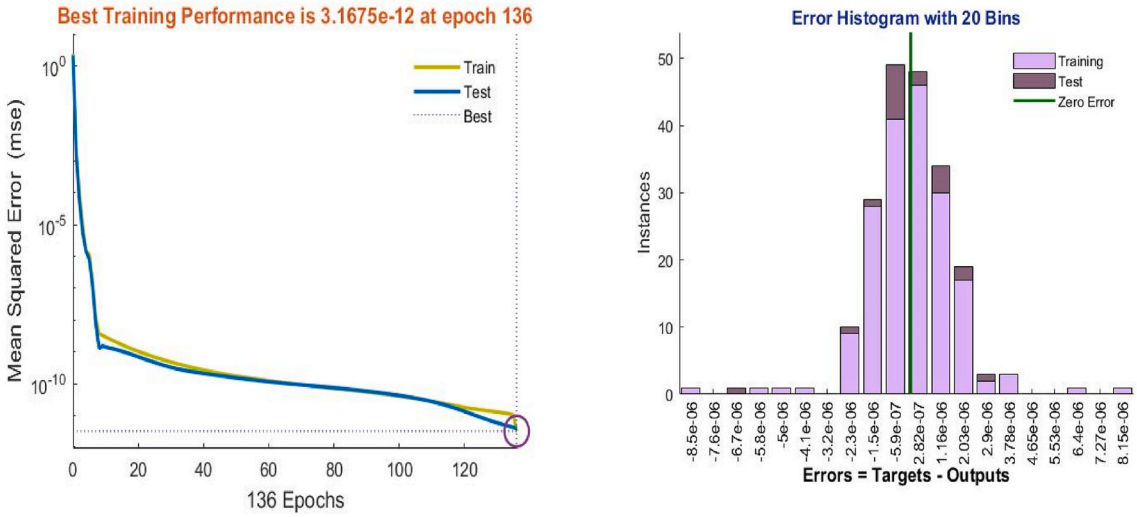

b. Scenario 2 Case 1

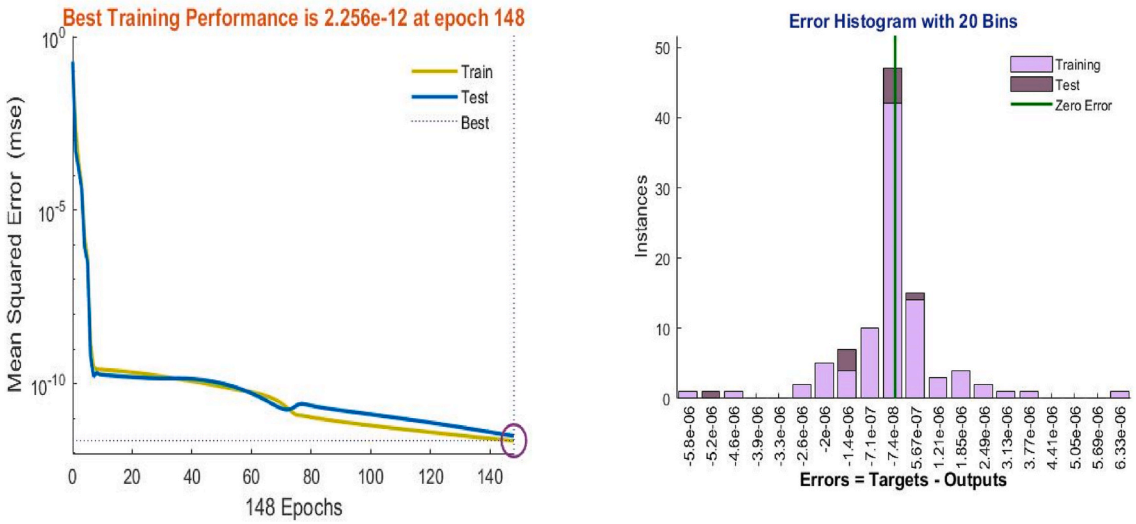

c. Scenario 3 Case 1

Fig. 5. Plots of MSE outcomes and error histogram for BRT-ANN of NMHD-CCNF

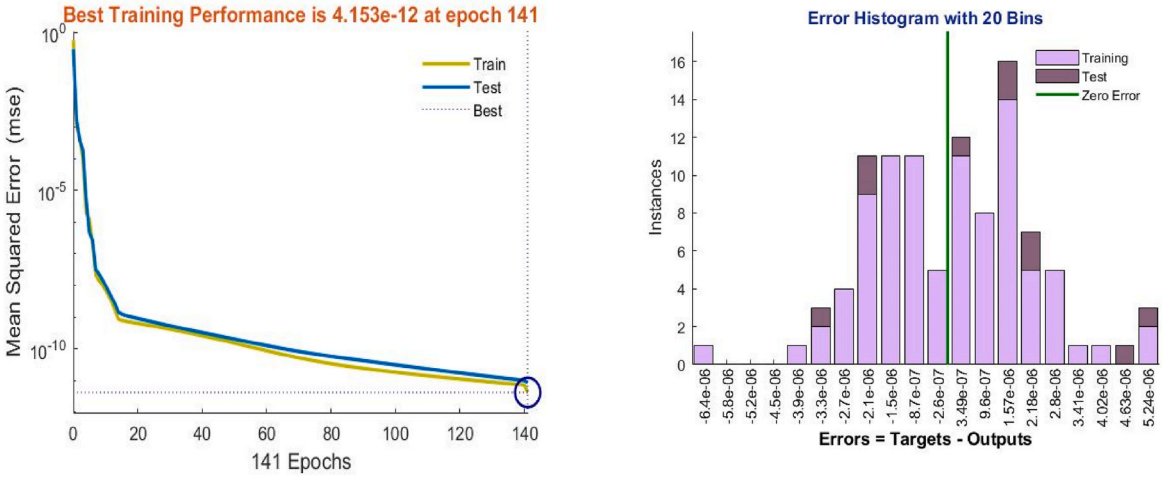

d. Scenario 4 Case 1

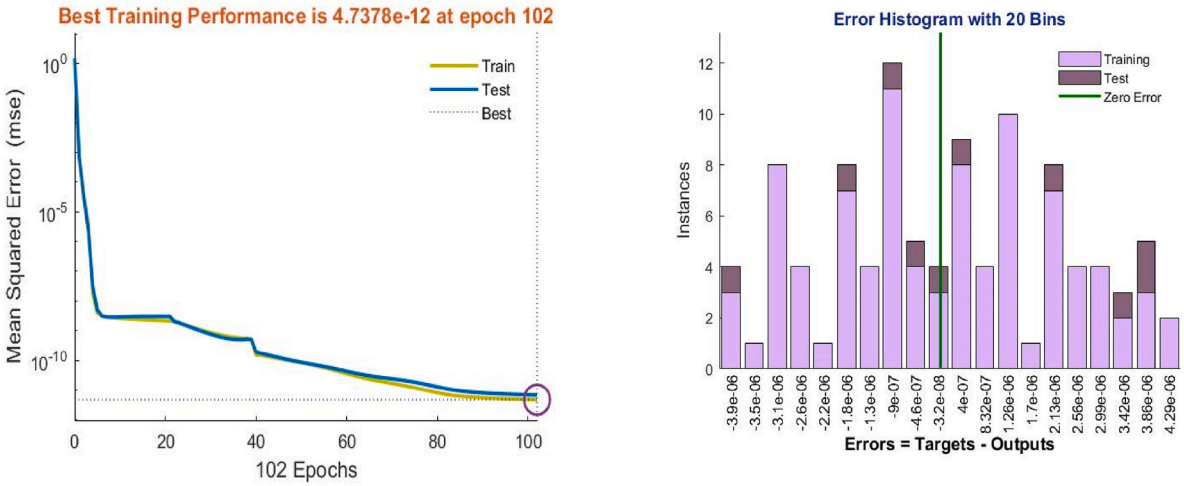

e. Scenario 5 Case 2

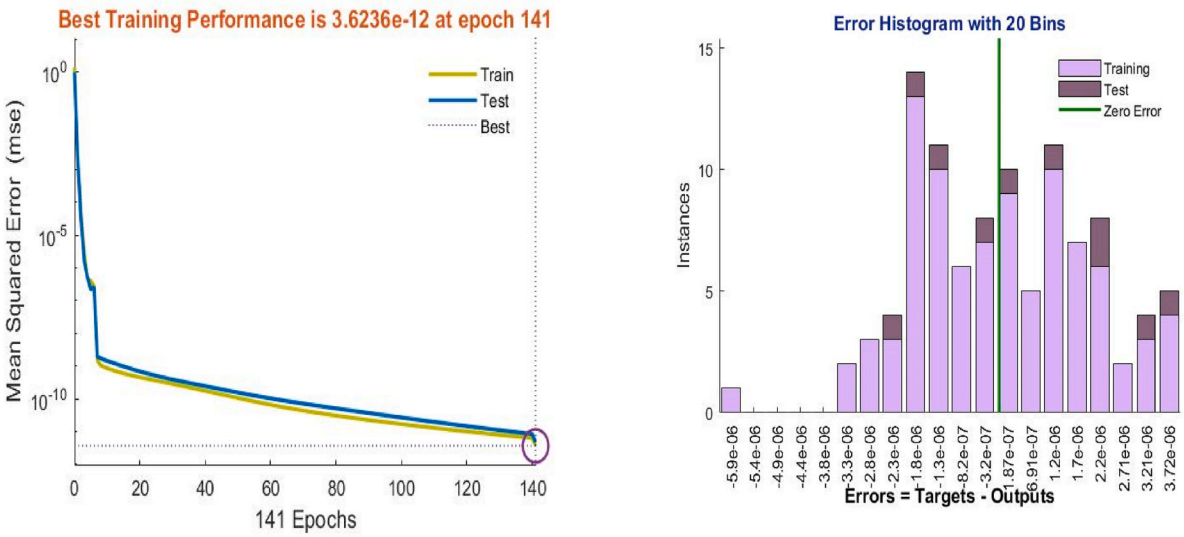

f. Scenario 6 Case 1

Fig. 5. (*continued*).

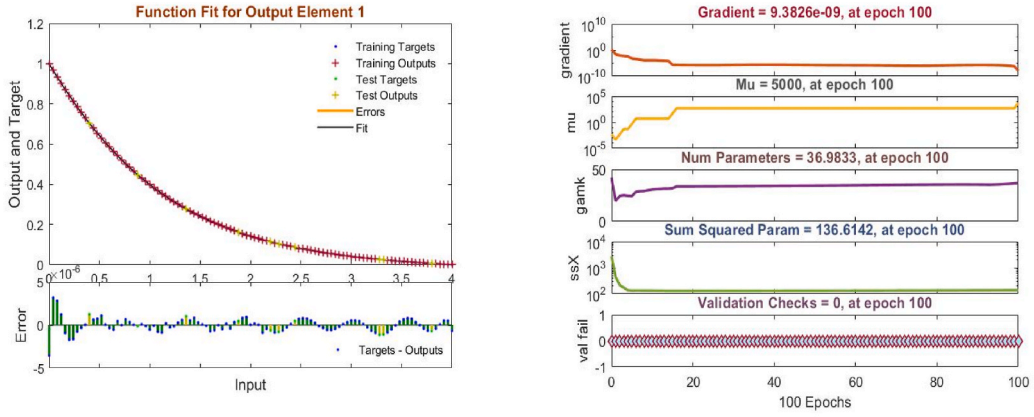

a. Scenario 1 Case 2

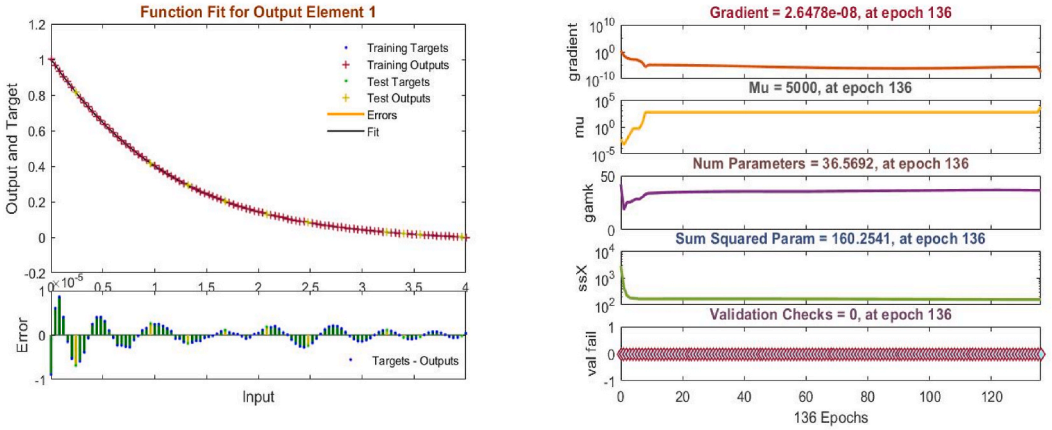

b. Scenario 2 Case 1

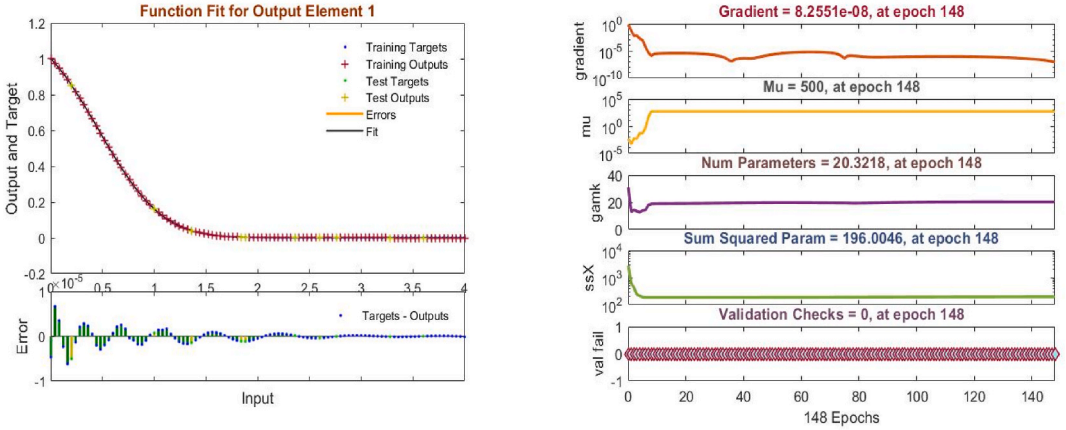

c. Scenario 3 Case 1

Fig. 6. Plots of Fitness curve and Transition state for BRT-ANN of NMHD-CCNF.

continuously through a variable wall concentration. The impacts of variable heat production, nonlinear thermal radiation, and Arrhenius activation energy are officially integrated into the planned two-phase nanofluidic flow pattern to strengthen the mass and heat transfer process inside the Casson nanofluidic media. The dimensionless forms of $L(\eta)$, $F(\eta)$, $\theta(\eta)$, $\varphi(\eta)$, C_f, Nu (it is used to calculate the heat transfer between the moving fluid flow and the surface in contact with the fluid. Moreover, it creates the linkages between convective and conductive heating impacts), and the Sherwood number Sh (it is used for mass transfer calculations. Moreover, it develops a linkage between convective mass transfer and rate of diffusive mass transfer), as shown in Figs. 8–11, Table 3, Table 4, and Table 5, have several graphical and numerical outcomes.

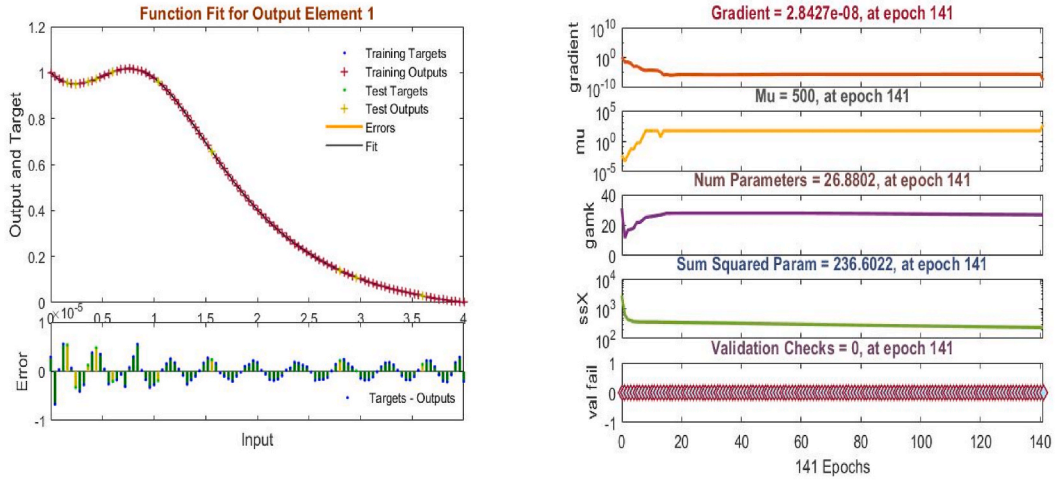

d. Scenario 4 Case 1

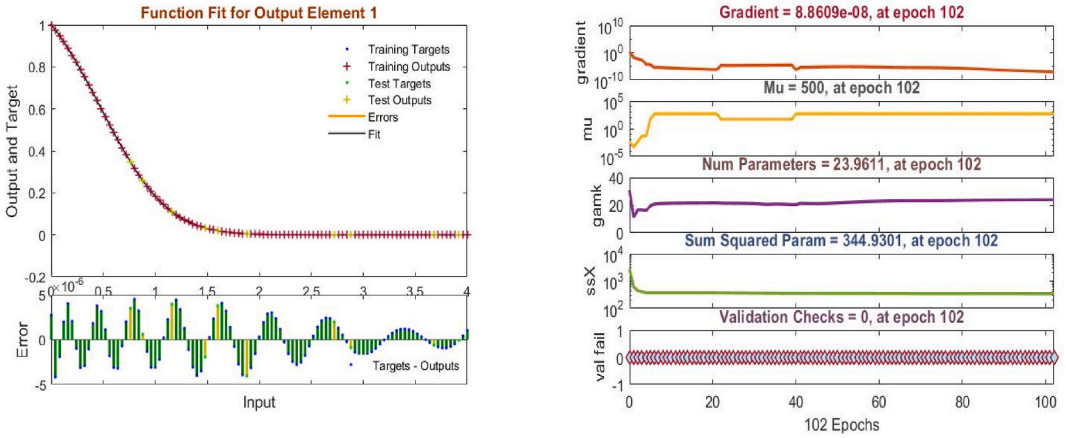

e. Scenario 5 Case 2

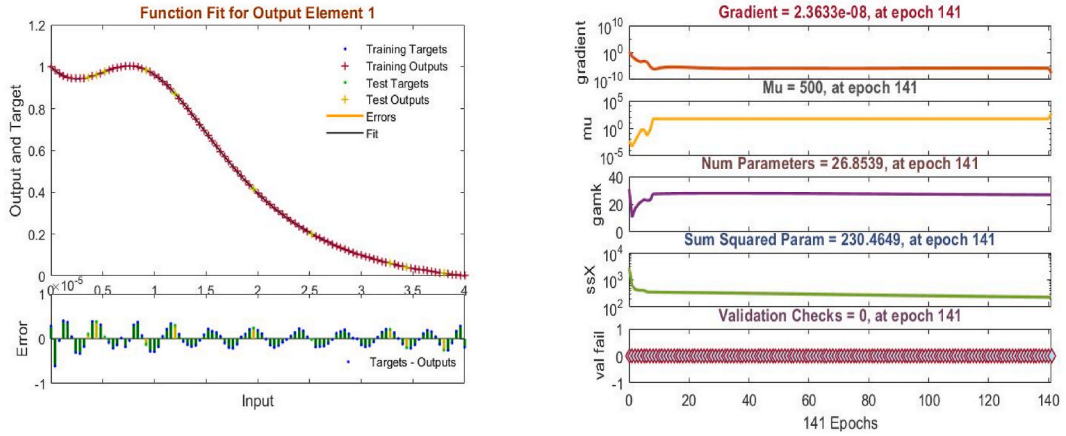

f. Scenario 6 Case 1

Fig. 6. (*continued*).

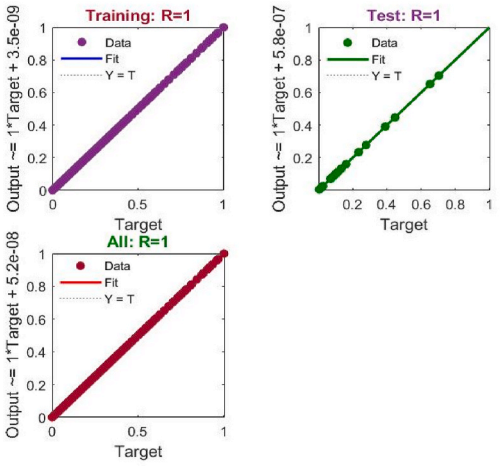

a. Scenario 1 Case 2

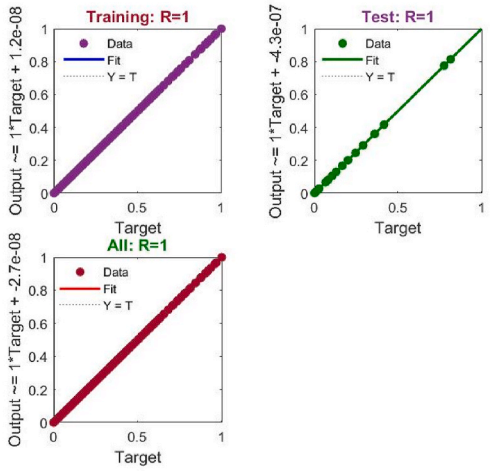

b. Scenario 2 Case 1

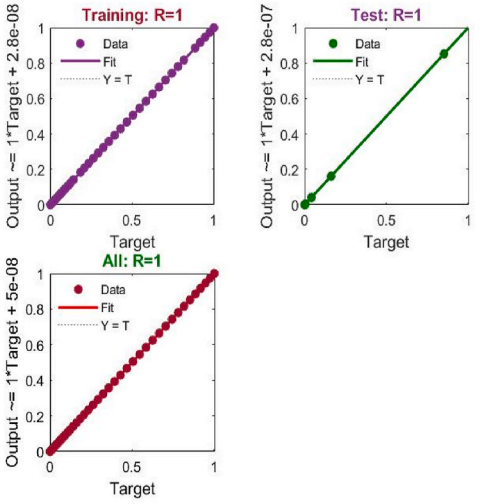

c. Scenario 3 Case 1

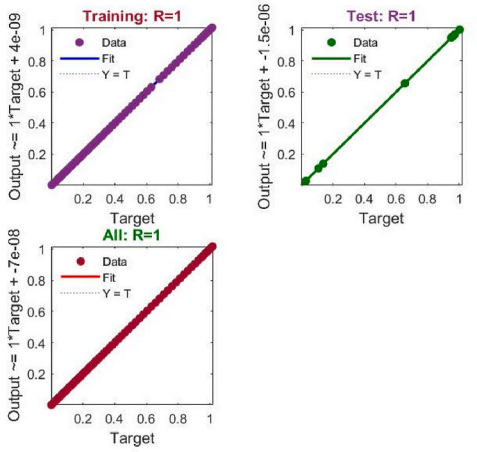

d. Scenario 4 Case 1

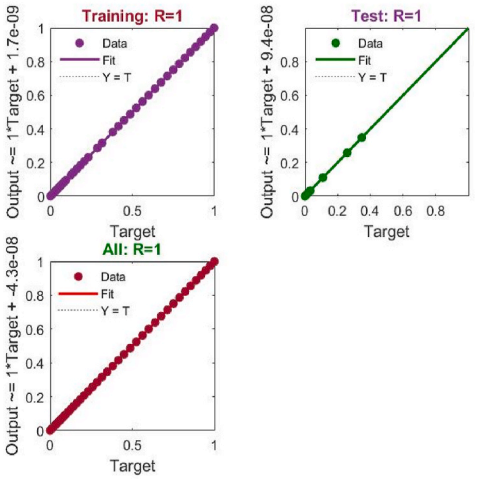

e. Scenario 5 Case 2

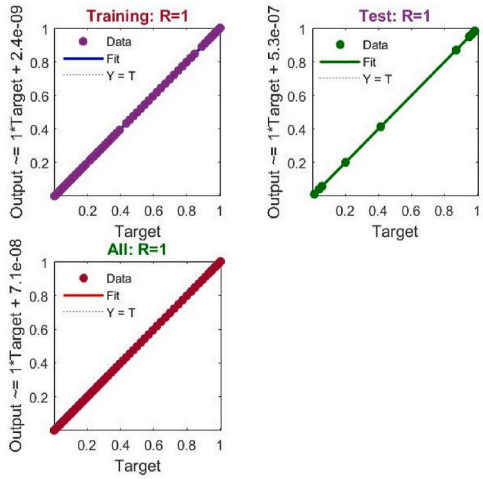

f. Scenario 6 Case 1

Fig. 7. Plots of regression for BRT-ANN of NMHD-CCNF

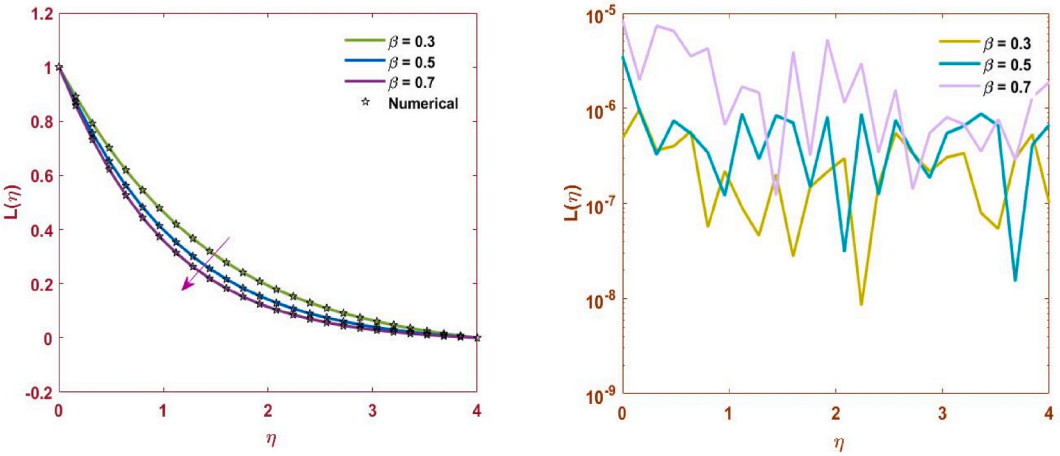

a. Solution & AE Plots of $L(\eta)$ for changing values of β

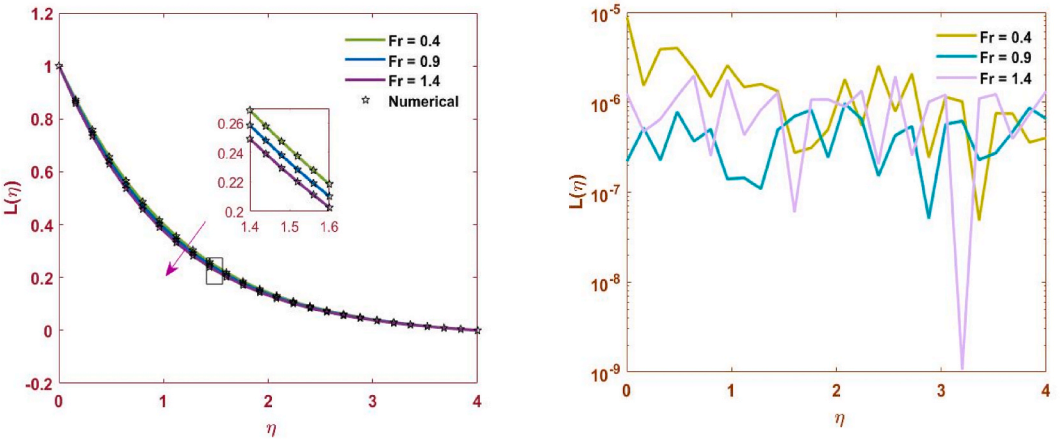

b. Solution & AE Plots of $L(\eta)$ for changing values of F_r

Fig. 8. Solution & AE plots for $L(\eta)$ of BRT-ANN

4.1. Radial and tangential velocity profiles ($L(\eta)$ and $F(\eta)$)

Figs. 8(a) and 9(a) show the effect of the Casson parameter β on the resultant three-dimensional nanofluid flow. These graphs indicate that β has a decreasing effect on the dynamical profiles related to $L(\eta)$ and $F(\eta)$ velocities. The cause for this is that when the Casson parameter β is estimated larger, the yield stress lessens tremendously. It's also worth noting that if the Casson parameter β is set to increasing values ($i.e., \beta \to \infty$), the Casson nanofluid acts rheological like a Newtonian nanofluid. As previously noted by Wakif [49], the nanofluidic medium's viscoelasticity trend has a delaying impact on nanofluid flow. As realized in Figs. 8(b) and Fig. 9(b), the drag forces of nonlinear Forchheimer that occur in the permeable material greatly increase the nanofluid flow resistance because of the amplification in the F_r.

4.1.1. Temperature profile ($\theta(\eta)$)

Brownian mass diffusion encourages ascending thermo-migration of nanoparticles inside the nanofluidic media [59]. It is important to note that the upward movement of nanoparticles helps to a certain extent the heat transfer rate inside the nanofluidic medium by enhancing $\theta(\eta)$ and bulking its corresponding boundary layer region. In terms of energy, the availability of an inner temperature-dependent source of heat, whose intensity can be controlled directly through the heat generation parameter Q_T, performs an increasing thermal function. As seen in Fig. 10(a), a specific heat is transferred non-uniformly throughout nanofluidic system, resulting in a significant increase in both the temperature distribution $\theta(\eta)$ and the thickness of the associated boundary layer. The thermal properties of the nanofluidic media (i.e., comparable thermal conductivity and diffusivity) improve when the thermal radiation parameter *Rd* is estimated more accurately. As a response of this thermal strength, $\theta(\eta)$, also the related boundary layer thickness, rises dramatically due to growing values of *Rd*, as seen in Fig. 10(b).

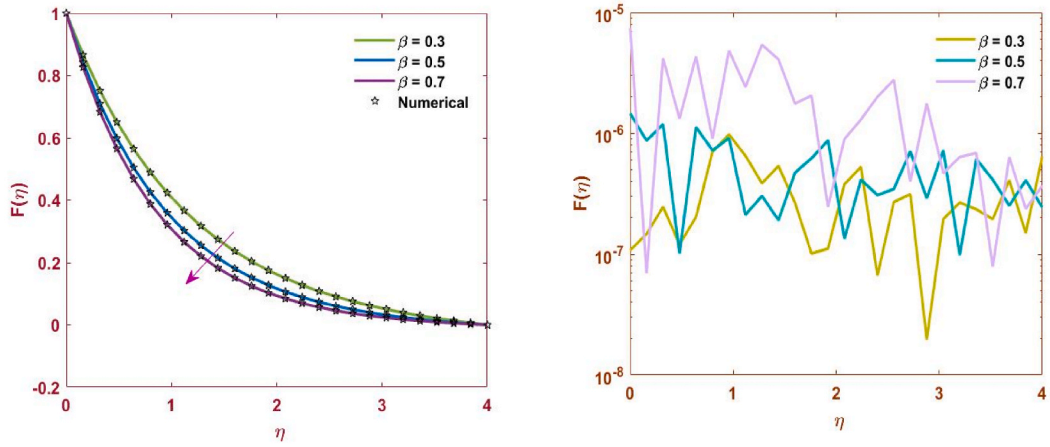

a. Solution & AE Plots of $F(\eta)$ for changing values of β

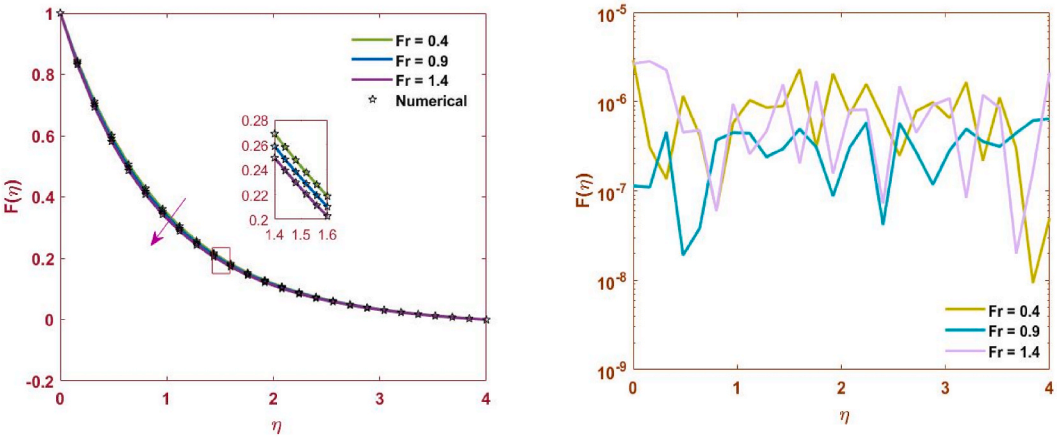

b. Solution & AE Plots of $F(\eta)$ for changing values of F_r

Fig. 9. Solution & AE plots for $F(\eta)$ of BRT-ANN

4.1.2. *Concentration profile ($\varphi(\eta)$)*

In light of the previous thermal observations mentioned in paper [59], it is noted that the thermophoresis procedure helps push supporting nanoparticles from the wall to the concentration boundary layer area, causing the nanofluidic channel to compress more, for which the mass amount of nanoparticles shifted ascendingly through the diffusion of thermophoretic process is fully rewarded to ensure that the wall concentration C_w remains constant. For detrimental chemical reactions, K_C is positive. The mass utilization of the reacting solid species is assisted by increasing chemical reaction parameter $\Lambda(=K_C/\Omega)$ in this scenario. As a result, if the chemical reaction process continues during the convective nanofluid flow, the concentration of the nanofluidic medium decreases gradually. As a result, against any quickest growing in Λ, $\varphi(\eta)$ and the concentration boundary layer thickness display a declining trend, as shown in Fig. 11 (b). During Arrhenius kinetics, the destructive tendency of Λ can be realistically slowed down by enhancing E sorted in the incredibly rapid reactive expression of the concentration equation, that creates a development in both $\varphi(\eta)$ and its related boundary layer thickness, as shown in Fig. 11 (a).

4.2. *Skin friction coefficient, nusselt number, and sherwood number (C_f, Nu, Sh)*

The table form outcomes in Tables 3–5 are derived from precise numerical data sources based on specified quantities $C_f, Nu,$ and Sh for varying values of the integrated control factors. Table 3 shows a measurable increase in C_f due to growing values of the parameters like the $a, P, F_r,$ and magnetic parameter M. The viscous frictional impact at the isothermal wall, on the other hand, shows a decreasing trend when β is increased. Table 4 shows that the increasing values of Γ and Rd result in an increase in Nu. The dimensionless thermal quantity $Nu,$ on the other hand, shows a decreasing trend when the parameters like heat generation parameter Q_T, $Nt,$ and Nb are evaluated greater. Regarding the behavior of the reduced Sh, Table 5 shows that its resultant wall mass transfer can be increased by increasing the amplitude of parameters such as the $Nb, \Lambda,$ and Sc or by reducing the power of parameters such as the Nt and activation energy parameter E.

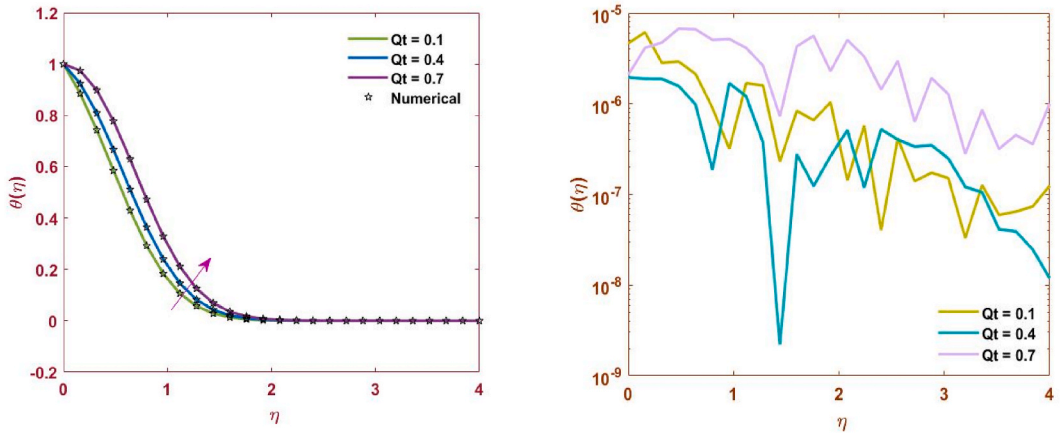

a. Solution & AE Plots of $\theta(\eta)$ for changing values of Q_T

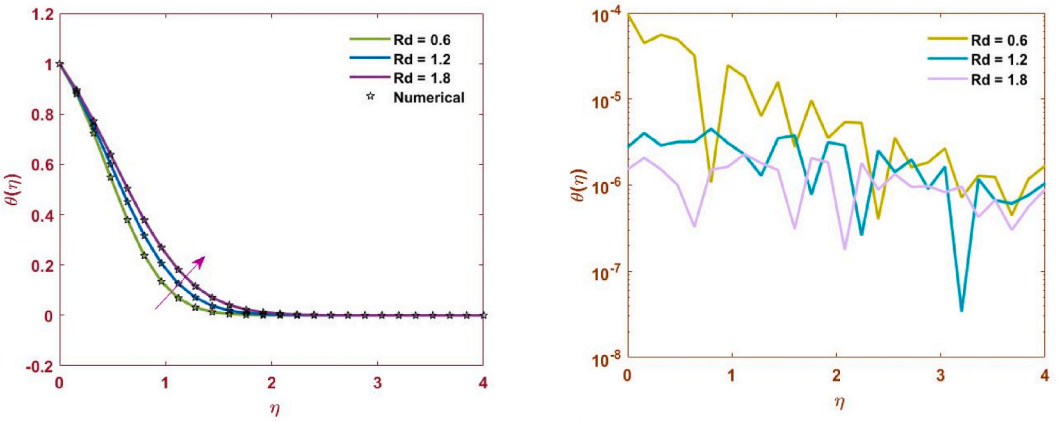

b. Solution & AE Plots of $\theta(\eta)$ for changing values of Rd

Fig. 10. Solution & AE plots for $\theta(\eta)$ of BRT-ANN

5. Conclusions

The present study examines the non-Darcian flow of Casson nanofluids across a radially extended spinning disc while considering a variety of flow characteristics by exploiting the strength of AI-based computing with the Bayesian Regularization technique of artificial neural networks. We can list the following important physical inferences drawn from the exhaustive simulation studies conducted by BRT-ANNs for the system:

- Both tangential and radial velocities show an opposite response against M, F_r, and P..
- Both tangential and radial velocities decrease with increase in values of Casson parameter β.
- An increase in stretching parameter a results an increase in radial velocity while tangential velocity decreases.
- The temperature profile is improved by the thermal radiation Rd and heat generation Q_T parameters.
- In temperature and concentration profiles, Nb has the opposite impact.
- As the value of Nt rises, so do the temperature and concentration profiles.
- The concentration profile decreases as the chemical reaction parameter Λ increases, although the Arrhenius activation energy parameter E increases significantly.
- The local skin friction coefficient is dominated by the non-Darcian phenomena, which includes the parameters like P and F_r.
- The higher the value of the parameter Rd, the better the rate of heat transmission through the wall.
- As the value of parameter E increases, the rate of wall mass transfer decreases.

In the future, one may investigate the proposed BRT-ANNs-based single network to model the approximate solutions of all reference results determined by 'ND-Solve' routine based on the numerical solution of the fluidic model NMHD-CCNF. Additionally, deep neural networks or/and deep learning procedures look promising to be investigated for improved modelling or approximation of outcomes of the NMHD-CCNF system.

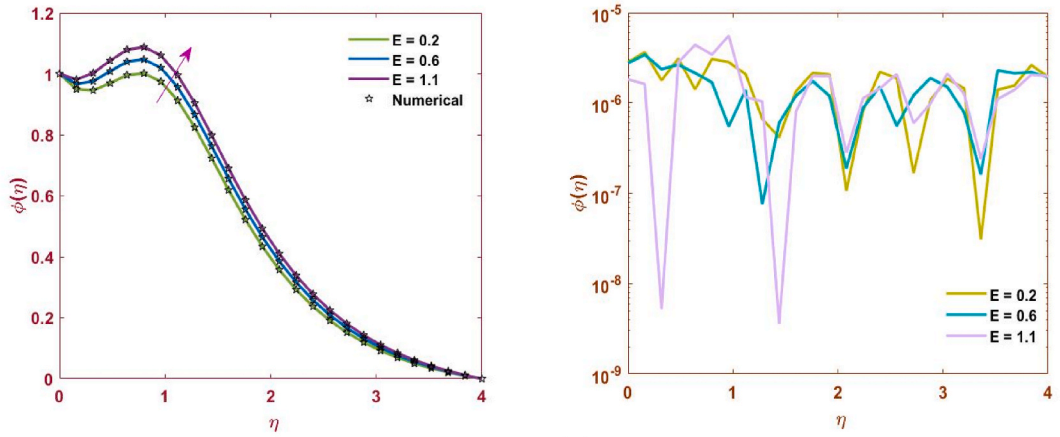

a. Solution & AE Plots of $\phi(\eta)$ for changing values of E

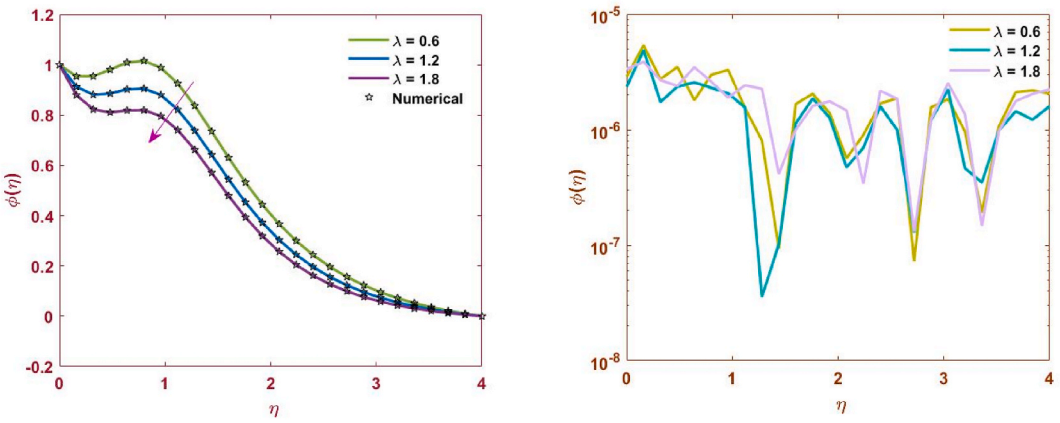

b. Solution & AE Plots of $\phi(\eta)$ for changing values of Λ

Fig. 11. Solution & AE plots for $\varphi(\eta)$ of BRT-ANN

Table 3
Outcomes of C_f for variation of $\alpha, \beta, P, F_r,$ and M.

Parameters	Default values	Changing values	C_f
α	1.0	0.4	2.6429418
		0.6	3.0268964
		0.8	3.5100369
		1.0	4.0862779
β	0.5	0.1	7.9690160
		0.2	5.8023112
		0.3	4.9174625
		0.4	4.4154024
P	0.5	0.5	4.0862779
		1.0	4.4255247
		1.5	4.7438369
		2.0	5.0440732
F_r	0.5	3	5.1212013
		6	6.1595133
		9	7.0551948
		12	7.8530529
M	0.5	0.5	4.0862779
		1.0	4.4255247
		1.5	4.7438369
		2.0	5.0440732

Table 4
Outcomes of Nu for variation of Q_T, Rd, Γ, Nt and Nb.

Parameters	Default values	Changing values	Nu
Q_T	0.1	0.0	1.9005521
		0.2	1.4623862
		0.4	0.9658089
		0.6	0.3843624
Γ	0.2	1.5	4.9529724
		2.0	6.3147552
		2.5	7.5585171
		3.0	8.5754714
Rd	1.0	0.5	1.1395850
		1.0	1.6876221
		1.5	2.1661628
		2.0	2.5904744
Nt	0.7	0.1	2.5025047
		0.2	2.3454271
		0.3	2.1973219
		0.4	2.0578496
Nb	0.5	0.8	1.2237162
		1.0	0.9667158
		1.2	0.7484198
		1.4	0.5656155

Table 5
Outcomes of Sh for variation of Nb, Nt, Sc, Λ and E.

Parameters	Default values	Changing values	Sh
Nt	0.7	0.1	0.6313299
		0.2	0.5487959
		0.3	0.4845293
		0.4	0.4366774
Nb	0.5	0.8	0.6374989
		1.0	0.7121742
		1.2	0.7541228
		1.4	0.7780140
Sc	0.5	5	3.0088390
		7	3.5651424
		10	4.2479096
		13	4.8242156
Λ	0.5	0.5	0.3748096
		1.0	0.6342345
		1.5	0.8448276
		2.0	1.0221547
E	0.5	0.1	0.4999604
		0.4	0.4031337
		0.7	0.3236885
		1.0	0.2596537

Data availability statement

Data will be made available on request.

CRediT authorship contribution statement

Muhammad Asif Zahoor Raja: Investigation, Methodology, Writing – original draft. **Kottakkaran Sooppy Nisar:** Investigation, Software, Writing – original draft, Writing – review & editing. **Muhammad Shoaib:** Conceptualization, Investigation, Software, Writing – original draft. **Marwan Abukhaled:** Formal analysis, Validation, Writing – review & editing. **Aqsa Riaz:** Investigation, Software, Visualization, Writing – original draft.

Declaration of competing interest

The authors declare that they have no known competing financial interests or personal relationships that could have appeared to influence the work reported in this paper.

Acknowledgement

"This study is supported via funding from Prince Sattam bin Abdulaziz University project number (PSAU/2023/R/1444)".

Appendix A. Supplementary data

Supplementary data to this article can be found online at https://doi.org/10.1016/j.heliyon.2023.e20911.

References

[1] S. Arrhenius, Quantitative relationship between the rate a reaction proceeds and its temperature, J. Phys. Chem. 4 (1889) 226–248.
[2] A.R. Bestman, Radiative heat transfer to flow of a combustible mixture in a vertical pipe, Int. J. Energy Res. 15 (3) (1991) 179–184.
[3] A.S. Mullin, H. Guo, A.B. McCoy, New physical insights from kinetics studies, J. Phys. Chem. 123 (14) (2019) 3057, 3057.
[4] M. Shoaib, M.A.Z. Raja, I. Farhat, Z. Shah, P. Kumam, S. Islam, Soft computing paradigm for Ferrofluid by exponentially stretched surface in the presence of magnetic dipole and heat transfer, Alex. Eng. J. 61 (2) (2022) 1607–1623.
[5] M.B. Arain, M.M. Bhatti, A. Zeeshan, T. Saeed, A. Hobiny, Analysis of arrhenius kinetics on multiphase flow between a pair of rotating circular plates, Math. Probl Eng. (2020) 2020.
[6] M. Shoaib, G. Zubair, K.S. Nisar, M.A.Z. Raja, M.I. Khan, R.P. Gowda, B.C. Prasannakumara, Ohmic heating effects and entropy generation for nanofluidic system of Ree-Eyring fluid: intelligent computing paradigm, Int. Commun. Heat Mass Tran. 129 (2021), 105683.
[7] T.L. Jensen, J.F. Moxnes, E. Unneberg, D. Christensen, Models for predicting impact sensitivity of energetic materials based on the trigger linkage hypothesis and Arrhenius kinetics, J. Mol. Model. 26 (4) (2020) 1–14.
[8] H. Waqas, S.A. Khan, M.M. Bhatti, S. Hussain, Bioconvection mechanism using third-grade nanofluid flow with Cattaneo–Christov heat flux model and Arrhenius kinetics, Int. J. Mod. Phys. B 35 (17) (2021), 2150178.
[9] L. Zhang, M.M. Bhatti, A. Shahid, R. Ellahi, O.A. Bég, S.M. Sait, Nonlinear nanofluid fluid flow under the consequences of Lorentz forces and Arrhenius kinetics through a permeable surface: a robust spectral approach, J. Taiwan Inst. Chem. Eng. 124 (2021) 98–105.
[10] K. Maleque, Effects of Binary Chemical Reaction and Activation Energy on MHD Boundary Layer Heat and Mass Transfer Flow with Viscous Dissipation and Heat Generation/absorption, International Scholarly Research Notices, 2013, 2013.
[11] K.A. Maleque, Unsteady natural convection boundary layer flow with mass transfer and a binary chemical reaction, Br. J. Appl. Sci. Technol. 3 (1) (2013) 131–149.
[12] K. Maleque, Effects of exothermic/endothermic chemical reactions with Arrhenius activation energy on MHD free convection and mass transfer flow in presence of thermal radiation, Journal of Thermodynamics (2013) 2013.
[13] A.M. Olanrewaju, S.O. Salawu, P.O. Olanrewaju, S.A. Amoo, Unsteady radiative magnetohydromagnetic flow and entropy generation of maxwell nanofluid in a porous medium with arrhenius chemical kinetic, Cogent Engineering 8 (1) (2021), 1942639.
[14] Bhatti, M. M., Abbas, T., Rashidi, M. M., Ali, M. E. S., & Yang, Z. Entropy generation on MHD Eyring–Powell nanofluid through a permeable stretching surface. Entropy, 18(6), 224..
[15] T.V. Karman, The analogy between fluid friction and heat transfer, Trans. Am. Soc. Mech. Eng. 61 (2016) (1939) 705–710.
[16] H.I. Andersson, E. De Korte, R. Meland, Flow of a power-law fluid over a rotating disk revisited, Fluid Dynam. Res. 28 (2) (2001) 75.
[17] Y.J. Lim, M.N. Zakaria, S.M. Isa, N.A.M. Zin, A.Q. Mohamad, S. Shafie, VON Kármán Casson fluid flow with Navier's slip and cattaneo-christov heat flux, Case Stud. Therm. Eng. 28 (2021), 101666.
[18] K.U. Rehman, M.Y. Malik, M. Zahri, M. Tahir, Numerical analysis of MHD Casson Navier's slip nanofluid flow yield by rigid rotating disk, Results in physics 8 (2018) 744–751.
[19] R. Kumar, R. Kumar, K. Vajravelu, M. Sheikholeslami, Three dimensional stagnation flow of Casson nanofluid through Darcy-Forchheimer space: a reduction to Blasius/Sakiadis flow, Chin. J. Phys. 68 (2020) 874–885.
[20] R.N. Kumar, F. Gamaoun, A. Abdulrahman, J.S. Chohan, R.P. Gowda, Heat transfer analysis in three-dimensional unsteady magnetic fluid flow of water-based ternary hybrid nanofluid conveying three various shaped nanoparticles: a comparative study, Int. J. Mod. Phys. B 36 (25) (2022), 2250170.
[21] J.C. Umavathi, D.G. Prakasha, Y.M. Alanazi, M.M. Lashin, F.S. Al-Mubaddel, R. Kumar, R.P. Gowda, Magnetohydrodynamic squeezing Casson nanofluid flow between parallel convectively heated disks, Int. J. Mod. Phys. B 37 (4) (2023), 2350031.
[22] K. Sarada, F. Gamaoun, A. Abdulrahman, S.O. Paramesh, R. Kumar, G.D. Prasanna, R.P. Gowda, Impact of exponential form of internal heat generation on water-based ternary hybrid nanofluid flow by capitalizing non-Fourier heat flux model, Case Stud. Therm. Eng. 38 (2022), 102332.
[23] M.S. Iqbal, M.W. Yasin, N. Ahmed, A. Akgül, M. Rafiq, A. Raza, Numerical simulations of nonlinear stochastic Newell-Whitehead-Segel equation and its measurable properties, J. Comput. Appl. Math. 418 (2023), 114618.
[24] Z. Iqbal, M.A.U. Rehman, M. Imran, N. Ahmed, U. Fatima, A. Akgül, F. Jarad, A finite difference scheme to solve a fractional order epidemic model of computer virus, AIMS Math 8 (2023) 2337–2359.
[25] N.A. Shah, I. Ahmed, K.K. Asogwa, A.A. Zafar, W. Weera, A. Akgül, Numerical study of a nonlinear fractional chaotic Chua's circuit, Aims Math 8 (2022) 1636–1655.
[26] A. Shahzad, M. Imran, M. Tahir, S.A. Khan, A. Akgül, S. Abdullaev, I.S. Yahia, Brownian motion and thermophoretic diffusion impact on Darcy-Forchheimer flow of bioconvective micropolar nanofluid between double disks with Cattaneo-Christov heat flux, Alex. Eng. J. 62 (2023) 1–15.
[27] Z.A. Qureshi, S. Bilal, U. Khan, A. Akgül, M. Sultana, T. Botmart, I.S. Yahia, Mathematical analysis about influence of Lorentz force and interfacial nano layers on nanofluids flow through orthogonal porous surfaces with injection of SWCNTs, Alex. Eng. J. 61 (12) (2022) 12925–12941.
[28] S. Bilal, I.A. Shah, A. Akgül, M.T. Tekin, T. Botmart, I.S. Yahia, A comprehensive mathematical structuring of magnetically effected Sutterby fluid flow immersed in dually stratified medium under boundary layer approximations over a linearly stretched surface, Alex. Eng. J. 61 (12) (2022) 11889–11898.
[29] I.A. Shah, S. Bilal, A. Akgül, M.T. Tekin, T. Botmart, H.Y. Zahran, I.S. Yahia, On analysis of magnetized viscous fluid flow in permeable channel with single wall carbon nano tubes dispersion by executing nano-layer approach, Alex. Eng. J. 61 (12) (2022) 11737–11751.
[30] Y. Ali, M. Afzal Rana, M. Shoaib, Three dimensional second grade fluid flow between two parallel horizontal plates with periodic suction/injection in slip flow regime, Punjab Univ. J. Math. 50 (4) (2020).
[31] W. Waseem, M. Sulaiman, P. Kumam, M. Shoaib, M.A.Z. Raja, S. Islam, Investigation of singular ordinary differential equations by a neuroevolutionary approach, PLoS One 15 (7) (2020), e0235829.
[32] U. Rashid, T. Abdeljawad, H. Liang, A. Iqbal, M. Abbas, M. Siddiqui, The shape effect of gold nanoparticles on squeezing nanofluid flow and heat transfer between parallel plates, Math. Probl Eng. (2020) 2020.
[33] A. Imran, R. Akhtar, Z. Zhiyu, M. Shoaib, M.A.Z. Raja, Analysis of MHD and heat transfer effects with variable viscosity through ductus efferentes, AIP Adv. 9 (8) (2019), 085320.
[34] H. Ilyas, I. Ahmad, M.A.Z. Raja, M. Shoaib, A novel design of Gaussian WaveNets for rotational hybrid nanofluidic flow over a stretching sheet involving thermal radiation, Int. Commun. Heat Mass Tran. 123 (2021), 105196.

[35] M. Shoaib, M.A.Z. Raja, M.T. Sabir, A.H. Bukhari, H. Alrabaiah, Z. Shah, S. Islam, A stochastic numerical analysis based on hybrid NAR-RBFs networks nonlinear SITR model for novel COVID-19 dynamics, Comput. Methods Progr. Biomed. 202 (2021), 105973.
[36] J.A. Carter, J.T. Sloop, T. Harville, B.T. Jones, G.L. Donati, Non-analyte signals and supervised learning to evaluate matrix effects and predict analyte recoveries in inductively coupled plasma optical emission spectrometry, Journal of Analytical Atomic Spectrometry 35 (4) (2020) 679–692.
[37] M.A.Z. Raja, A. Mehmood, A.A. Khan, A. Zameer, Integrated intelligent computing for heat transfer and thermal radiation-based two-phase MHD nanofluid flow model, Neural Comput. Appl. 32 (7) (2020) 2845–2877.
[38] Y. Chen, C. Schmid, C. Sminchisescu, Self-supervised learning with geometric constraints in monocular video: connecting flow, depth, and camera, in: Proceedings of the IEEE/CVF International Conference on Computer Vision, 2019, pp. 7063–7072.
[39] Z. Shah, M.A.Z. Raja, Y.M. Chu, W.A. Khan, M. Waqas, M. Shoaib, S.Z. Abbass, Design of neural network based intelligent computing for neumerical treatment of unsteady 3D flow of Eyring-Powell magneto-nanofluidic model, J. Mater. Res. Technol. 9 (6) (2020) 14372–14387.
[40] I. Ahmad, H. Ilyas, A. Urooj, M.S. Aslam, M. Shoaib, M.A.Z. Raja, Novel applications of intelligent computing paradigms for the analysis of nonlinear reactive transport model of the fluid in soft tissues and microvessels, Neural Comput. Appl. 31 (12) (2019) 9041–9059.
[41] J. Buongiorno, Convective Transport in Nanofluids, 2006.
[42] H. Schlichting, K. Gersten, Fundamentals of boundary-layer theory, in: Boundary-Layer Theory, Springer, Berlin, Heidelberg, 2000, pp. 29–49.
[43] A. Wakif, I.L. Animasaun, U. Khan, A.M. Alshehri, Insights into the Generalized Fourier's and Fick's Laws for Simulating Mixed Bioconvective Flows of Radiative-Reactive Walters-B Fluids Conveying Tiny Particles Subject to Lorentz Force, 2021.
[44] S.M. Upadhya, R.L.V. Devi, C.S.K. Raju, H.M. Ali, Magnetohydrodynamic nonlinear thermal convection nanofluid flow over a radiated porous rotating disk with internal heating, J. Therm. Anal. Calorim. 143 (3) (2021) 1973–1984.
[45] I. Ullah, R. Ullah, M.S. Alqarni, W.F. Xia, T. Muhammad, Combined heat source and zero mass flux features on magnetized nanofluid flow by radial disk with the applications of Coriolis force and activation energy, Int. Commun. Heat Mass Tran. 126 (2021), 105416.
[46] S. Rosseland, Springer-verlag; Berlin, Astrophysik und atom-theoretische Grundlagen, 1931.
[47] T. Von Kármán, Uber laminare und turbulente Reibung, Z. Angew. Math. Mech. 1 (1921) 233–252.
[48] A. Tassaddiq, S. Khan, M. Bilal, T. Gul, S. Mukhtar, Z. Shah, E. Bonyah, Heat and mass transfer together with hybrid nanofluid flow over a rotating disk, AIP Adv. 10 (5) (2020), 055317.
[49] A. Wakif, A novel numerical procedure for simulating steady MHD convective flows of radiative Casson fluids over a horizontal stretching sheet with irregular geometry under the combined influence of temperature-dependent viscosity and thermal conductivity, Math. Probl Eng. (2020) 2020.
[50] M. Shoaib, M.A.Z. Raja, M.T. Sabir, S. Islam, Z. Shah, P. Kumam, H. Alrabaiah, Numerical investigation for rotating flow of MHD hybrid nanofluid with thermal radiation over a stretching sheet, Sci. Rep. 10 (1) (2020) 1–15.
[51] J.L. Aljohani, E.S. Alaidarous, M.A.Z. Raja, M. Shoaib, M.S. Alhothuali, Intelligent computing through neural networks for numerical treatment of non-Newtonian wire coating analysis model, Sci. Rep. 11 (1) (2021) 1–32.
[52] I. Uddin, I. Ullah, M.A.Z. Raja, M. Shoaib, S. Islam, M.S. Zobaer, K.S. Nisar, C.A. Saleel, S. Alshahrani, The intelligent networks for double-diffusion and MHD analysis of thin film flow over a stretched surface, Sci. Rep. 11 (1) (2021) 1–20.
[53] M. Awais, M. Shoaib, M.A.Z. Raja, S. Arif, M.Y. Malik, K.S. Nisar, K.A. Ismail, Endoscopy applications for the second law analysis in hydromagnetic peristaltic nanomaterial rheology, Sci. Rep. 12 (1) (2022) 1–14.
[54] M.A.Z. Raja, M. Sabati, N. Parveen, M. Awais, S.E. Awan, N.I. Chaudhary, M. Shoaib, H. Alquhayz, Integrated intelligent computing application for effectiveness of Au nanoparticles coated over MWCNTs with velocity slip in curved channel peristaltic flow, Sci. Rep. 11 (1) (2021) 1–20.
[55] M. Abukhaled, S.A. Khuri, A fast convergent semi-analytic method for an electrohydrodynamic flow in a circular cylindrical conduit, Int. J. Algorithm. Comput. Math. 7 (2021) 1–15.
[56] M. Shoaib, M. Abukhaled, M.A.R. Raja, M.A.Z. Khan, M.T. Sabir, K.S. Nisar, I. Iltaf, Heat and mass transfer analysis for unsteady three-dimensional flow of hybrid nanofluid over a stretching surface using supervised neural networks, Frontiers in Physics 10 (2022), 949907.
[57] S.T. Suganya, P. Balaganesan, L. Rajendran, M. Abukhaled, Analytical discussion and sensitivity analysis of parameters of magnetohydrodynamic free convective flow in an inclined plate, European Journal of Pure and Applied Mathematics 13 (3) (2020) 631–644.
[58] M. Abukhaled, Green's function iterative method for Solving a class of boundary value problems arising in heat transfer, Applied Mathematics and Information Sciences 11 (1) (2017) 229–234.
[59] M. Shoaib, A. Riaz, M.A.Z. Raja, K.S. Nisar, Computational Intelligence for MHD Mixed Convection Williamson Fluid Flow along a Stretched Surface under Dufour and Soret Impacts. Waves in Random and Complex Media, 2022, pp. 1–34.